The MUSIC of galaxy clusters – II. X-ray global properties and scaling relations

V. Biffi,[1,2]★ F. Sembolini,[1,3] M. De Petris,[3] R. Valdarnini,[2,4] G. Yepes[1] and S. Gottlöber[5]

[1]*Departamento de Física Teorica, Universidad Autónoma de Madrid, Ciudad Universitaria de Cantoblanco, E-28049 Madrid, Spain*
[2]*SISSA – Scuola Internazionale Superiore di Studi Avanzati, Via Bonomea 265, I-34136 Trieste, Italy*
[3]*Dipartimento di Fisica, Sapienza Universitá di Roma, Piazzale Aldo Moro 5, I-00185 Roma, Italy*
[4]*INFN – Iniziativa Specifica QGSKY, Via Valerio 2, I-34127 Trieste, Italy*
[5]*Leibniz-Institut für Astrophysik, An der Sternwarte 16, D-14482 Potsdam, Germany*

ABSTRACT

We present the X-ray properties and scaling relations of a large sample of clusters extracted from the Marenostrum MUltidark SImulations of galaxy Clusters (MUSIC) data set. We focus on a sub-sample of 179 clusters at redshift $z \sim 0.11$, with $3.2 \times 10^{14}\, h^{-1}\, M_\odot < M_{\rm vir} < 2 \times 10^{15}\, h^{-1}\, M_\odot$, complete in mass. We employed the X-ray photon simulator PHOX to obtain synthetic *Chandra* observations and derive observable-like global properties of the intracluster medium (ICM), as X-ray temperature ($T_{\rm X}$) and luminosity ($L_{\rm X}$). $T_{\rm X}$ is found to slightly underestimate the true mass-weighted temperature, although tracing fairly well the cluster total mass. We also study the effects of $T_{\rm X}$ on scaling relations with cluster intrinsic properties: total (M_{500} and gas $M_{g,500}$ mass; integrated Compton parameter ($Y_{\rm SZ}$) of the Sunyaev-Zel'dovich (SZ) thermal effect; $Y_{\rm X} = M_{g,500}\, T_{\rm X}$. We confirm that $Y_{\rm X}$ is a very good mass proxy, with a scatter on $M_{500}-Y_{\rm X}$ and $Y_{\rm SZ}-Y_{\rm X}$ lower than 5 per cent. The study of scaling relations among X-ray, intrinsic and SZ properties indicates that simulated MUSIC clusters reasonably resemble the self-similar prediction, especially for correlations involving $T_{\rm X}$. The observational approach also allows for a more direct comparison with real clusters, from which we find deviations mainly due to the physical description of the ICM, affecting $T_{\rm X}$ and, particularly, $L_{\rm X}$.

Key words: hydrodynamics – methods: numerical – galaxies: clusters: intracluster medium – X-rays: galaxies: clusters.

1 INTRODUCTION

In the last decades, X-ray observations of galaxy clusters have continuously provided us with precious information on their intrinsic properties and components. In particular, the X-ray emission from the diffuse intracluster medium (ICM) has been proved to be a good tracer of both the physics governing the gaseous component and the characteristics of the underlying potential well, basically dominated by the non-luminous, dark matter (see Sarazin 1986).

A reliable estimate of their total mass represents a fundamental goal of astrophysical and cosmological investigations, as the accurate weighing of clusters is also crucial to use them as cosmological probes, e.g. via number counts (see e.g. Allen, Evrard & Mantz 2011, and references therein). In the X-ray band, clusters are very bright sources relatively easy to detect out to high redshifts and con-

stitute therefore a powerful tool to select large samples of objects for cosmology studies. However, the mass determination via X-ray observations is mainly possible for well-resolved, regular, nearby galaxy clusters, for which ICM density and temperature profiles are measurable with good precision and the Hydrostatic Equilibrium hypothesis can be safely applied.

As widely discussed in the literature (Rasia et al. 2006; Nagai, Vikhlinin & Kravtsov 2007; Lau, Kravtsov & Nagai 2009; Meneghetti et al. 2010; Suto et al. 2013), the hydrostatic mass can misestimate the true total mass by a factor up to 20–30 per cent, due to underlying erroneous assumptions (e.g. on the dynamical state of the system, on the ICM non-thermal pressure support, on the models used to deproject observed density and temperature profiles or on cluster sphericity).

In many cases, especially at high redshift or for more disturbed, irregular systems, when the hydrostatic X-ray mass cannot be inferred reliably, mass proxies are commonly employed to obtain indirect mass estimates. Scaling relations between global cluster properties

★ E-mail: biffi@sissa.it

can be invoked to this purpose, offering a substitute approach to derive the total mass from other observables, e.g. obtained from the X-ray band or through the thermal Sunyaev Zel'dovich (SZ; Sunyaev & Zeldovich 1970, 1972) effect.

In fact, the simple scenario of the gravitational collapse, by which gravity is dominating the cluster formation process, predicts a self-similar scaling of basic cluster observables with their mass (Kaiser 1986). Observations of galaxy clusters have confirmed the presence of correlations among cluster properties, and with mass, although indicating in some cases a certain level of deviation from the expected self-similar slopes. The main reason for this deviation is that non-gravitational processes on smaller scales (e.g. cooling, dynamical interactions, feedback from active galactic nuclei – AGN) do take place during the assembly of clusters and have a non-negligible effect on their energy content. In this respect, a remarkable example is represented by the X-ray luminosity–temperature relation, which is commonly observed to be significantly steeper than expected (White, Jones & Forman 1997; Markevitch 1998; Arnaud & Evrard 1999; Ikebe et al. 2002; Ettori et al. 2004b; Maughan 2007; Zhang et al. 2008; Pratt et al. 2009).

In order to employ scaling relations to infer masses, also the scatter about the relations has to be carefully considered: the tighter the correlation, the more precise can be the mass estimate. Therefore, investigating the intrinsic scatter that possibly exists for correlation with certain properties is extremely useful in order to individuate the lowest-scatter mass proxy among many observable properties (e.g. Ettori et al. 2012). This is the case, for instance, of the integrated Compton parameter, Y_{SZ}, a measure of the thermal SZ signal which has been confirmed to closely trace the cluster total mass by both simulations and observations (da Silva et al. 2004; Nagai 2006; Morandi, Ettori & Moscardini 2007; Bonamente et al. 2008; Comis et al. 2011; Kay et al. 2012; Planck Collaboration 2013; Sembolini et al. 2013a). The physical motivation for this is that Y_{SZ} is related to the ICM pressure (integrated along the line of sight), or equivalently to its total thermal energy, and thus to the depth of the cluster potential well. Likewise, another remarkably good candidate is also the X-ray-analogue of the Y_{SZ} parameter, Y_X, which was introduced by Kravtsov, Vikhlinin & Nagai (2006) and similarly quantifies the ICM thermal energy by the product of gas mass and spectroscopic temperature. Therefore, Y_X correlates strictly with Y_{SZ}, but also with total mass, given a fortunate anticorrelation of the residuals in temperature and gas mass.

As widely explored in the literature, numerical hydrodynamical simulations can be as precious as observations in unveiling the effects of a number of physical processes on the global properties and self-similar appearance of galaxy clusters (see e.g. recent reviews by Borgani & Kravtsov 2011; Kravtsov & Borgani 2012). Current hydrodynamical simulations can further be exploited when results are obtained in an observational fashion, which makes the results more directly comparable to real data, e.g. from the X-ray band (e.g. Mathiesen & Evrard 2001; Gardini et al. 2004; Mazzotta et al. 2004; Rasia et al. 2005, 2006; Kravtsov et al. 2006; Valdarnini 2006; Nagai et al. 2007; Jeltema et al. 2008; Biffi et al. 2012; Biffi, Dolag & Böhringer 2013a,b) or weak lensing (e.g. Meneghetti et al. 2010; Rasia et al. 2012). Under this special condition, projection and instrumental effects, unavoidable in real observations, can be limited and explored for the ideal case of simulated clusters, as the intrinsic properties can be calculated exactly from the simulation.

In return, simulations themselves can take advantage of such technique, as mismatches between theoretical definitions of observable properties, used in numerical studies, can be overcome (see e.g. studies on the ICM X-ray temperature by Mazzotta et al. 2004;

Valdarnini 2006; Nagai et al. 2007) and the capability of the implemented physical descriptions to match real clusters can be better constrained (e.g. Puchwein, Sijacki & Springel 2008; Fabjan et al. 2010, 2011; Biffi et al. 2013b; Planelles et al. 2014).

This is the approach we intend to follow in this work. Specifically, we study the Marenostrum MUltidark SImulations of galaxy Clusters (MUSIC) data set of cluster re-simulations by means of synthetic X-ray observations obtained with the virtual photon simulator PHOX (Biffi et al. 2012). The scope of this analysis is to extend the study carried on by Sembolini et al. (2013a) to the X-ray features and scaling relations of the MUSIC clusters, thereby providing a more complete picture of this simulated set with respect to their baryonic properties. In fact, X-ray observables are highly susceptible to the complexity of the ICM physical state (e.g. to its multiphase structure) and can be more significantly affected by the numerical description of the baryonic processes accounted for in the simulations (particularly cooling, star formation and feedback mechanisms).

The paper is organized as follows.

In Section 2, we present the sub-sample of simulated objects considered for the present study, whereas the generation and analysis of synthetic X-ray observations are described in Section 3. In Section 4, we discuss the main results. Specifically, X-ray observables are analysed and compared to theoretical estimates derived directly from the simulations (Section 4.1). In Section 4.2, we present instead mass-observable correlations (Sections 4.2.1–4.2.3), as well as pure X-ray (Section 4.2.4) and mixed X-ray/SZ (Sections 4.2.5–4.2.7) scaling relations. These are analysed and discussed with respect to the effects of the observational-like approach, the X-ray temperature determination, the compatibility with the expected self-similar scenario and the comparison against observational and previous numerical findings (Section 4.2.8).

Finally, we draw our conclusions in Section 5.

2 SIMULATED SAMPLE OF GALAXY CLUSTERS

The numerical simulations employed in this work are part of the MUSIC project, in particular of the MultiDark sub-set of re-simulated galaxy clusters (MUSIC-2, see Sembolini et al. 2013a).

The MultiDark simulation (MD) is a dark-matter-only *N*-body simulation performed with the adaptive refinement tree (ART) code (Kravtsov, Klypin & Khokhlov 1997), resolved with 2048^3 particles in a $(1\,h^{-1}\,\text{Gpc})^3$ volume (Prada et al. 2012). The cosmology assumed refers to the best-fitting parameters obtained from the *WMAP*7+BAO+SNI data, i.e. $\Omega_{M,0} = 0.27$, $\Omega_b = 0.0469$, $\Omega_{\Lambda,0} = 0.73$, $h_0 = 0.7$, $\sigma_8 = 0.82$ and $n = 0.95$ (Komatsu et al. 2011).

MUSIC-2 re-simulated clusters: a complete, mass-selected, volume-limited sample of 282 clusters has been extracted from a low-resolution (256^3 particles) run of the MD simulation. Namely, it comprises all the systems in the $(1\,h^{-1}\,\text{Gpc})^3$ volume with virial mass larger than $10^{15}\,h^{-1}\,\text{M}_\odot$ at redshift $z = 0$.

Each one of the identified systems has been then re-simulated with higher resolution and including hydrodynamics, within a radius of $6\,h^{-1}$ Mpc from the centre of each object at $z = 0$. Initial conditions for the re-simulations were generated with the zooming technique by Klypin et al. (2001). The re-simulations were performed with the TreePM/SPH parallel code GADGET (Springel, White & Hernquist 2001; Springel 2005), including treatments for cooling, star formation and feedback from SNe winds (Springel & Hernquist 2003). The final mass resolution for these re-simulations

is $m_{DM} = 9.01 \times 10^8 \, h^{-1} \, M_\odot$ and $m_{gas} = 1.9 \times 10^8 \, h^{-1} \, M_\odot$, respectively.

This permitted to obtain a huge catalogue of cluster-like haloes, namely more than 500 objects more massive than $10^{14} \, h^{-1} \, M_\odot$ at redshift zero.

Snapshots corresponding to 15 different redshifts have been stored between $z = 9$ and $z = 0$.[1]

2.1 The simulated data set

The sub-sample of re-simulated galaxy clusters for which we want to analyse X-ray properties is selected from the MUSIC-2 data set employed in the work presented by Sembolini et al. (2013a).

For the present analysis, we focus in particular on one snapshot at low redshift, i.e. $z = 0.11$. This redshift corresponds to one of the first time records of the simulation output earlier than $z = 0$[2] and is suitable to investigate cluster properties in a relatively recent epoch with respect to the early stages of formation.

Precisely, we select all the clusters matching the mass completeness of the MUSIC-2 data set at this redshift (see Sembolini et al. 2013a), i.e. $M_{vir}(z = 0.11) > 7.5 \times 10^{14} \, h^{-1} \, M_\odot$. Additionally, we also enlarge the sub-sample in order to comprise all the progenitors at $z = 0.11$ of the systems with virial masses above the completeness mass limit at $z = 0$ ($M_{vir}(z = 0) > 8.5 \times 10^{14} \, h^{-1} \, M_\odot$). This practically extends the $z = 0.11$ selection towards the intermediate-mass end.

As a result, we obtain a volume-limited sample of 179 clusters that is complete in mass at $z = 0.11$, with $M_{vir}(z = 0.11)$ spanning the range $[3.2 - 20] \times 10^{14} \, h^{-1} \, M_\odot$.

3 THE SYNTHETIC X-RAY OBSERVATIONS WITH PHOX

Synthetic X-ray observations of the galaxy clusters of the selected sample have been performed by means of the X-ray photon simulator PHOX (see Biffi et al. 2012 for an extensive presentation of the implemented approach).

The cube of virtual photons associated with each cluster box has been generated for the simulated snapshot at redshift $z = 0.11$.

For each gas element in the simulation, X-ray emission has been derived by calculating a theoretical spectral model with the X-ray-analysis package XSPEC[3] (Arnaud 1996). In particular, we assumed the thermal APEC model (Smith et al. 2001), and also combined this with an absorption model, WABS (Morrison & McCammon 1983), in order to mimic the suppression of low-energy photons due to Galactic absorption. To this purpose, the equivalent hydrogen column density parameter has been fixed to the fiducial value of $N_H = 10^{20} \, cm^{-2}$. Temperature, total metallicity and density of each gas element, required to calculate the spectral emission model, have been directly obtained from the hydrodynamical simulation output.

At this stage, fiducial, ideal values for collecting area and observation time have been assumed, namely $A_{fid} = 1000 \, cm^2$ and $\tau_{exp,fid} = 1 \, Ms$.

For the geometrical selection, we have considered a cylinder-like region enclosed by the R_{500} radius around each cluster. The radius R_{500} is here defined as the radius encompassing a region with an overdensity of $\Delta_{cr} = 500$, with respect to the *critical* density of the Universe, and in the following we will always use this definition when referring to R_{500}. This choice is motivated by our intention of comparing against the majority of the observational and numerical works in the literature, which commonly adopt the same overdensity. As for the projection, we consider a line of sight (l.o.s.) aligned with the z-axis of the simulation box.

Finally, we assume a realistic exposure time of $100 \, ks$ and perform synthetic observations for the ACIS-S detector of *Chandra*. This is done with PHOX Unit-3, by convolving the ideal photon lists extracted from the selected regions with the ancillary response file (ARF) and the redistribution matrix file (RMF) of the ACIS-S detector.

Given the adopted cosmology, the 17 arcsec × 17 arcsec field of view of *Chandra* corresponds at our redshift to a region in the sky of 2062.44 kpc per side (physical units), which would not comprise the whole R_{500} region for the majority of the clusters in the sample. Nevertheless, one can always assume to be ideally able to entirely cover each cluster with multiple-pointing observations, and therefore, we profit from the simulation case to extract X-ray properties from within R_{500} for all the objects.

3.1 X-ray analysis of *Chandra* synthetic spectra

The synthetic *Chandra* spectra generated with PHOX have been re-grouped requiring a minimum of 20 counts per energy bin. Spectral fits of the synthetic *Chandra* spectra, corresponding to the R_{500} region of each cluster, have been performed over the $0.5 - 10 \, keV$ energy band[4] by using XSPEC and adopting an absorbed (WABS), thermally broadened, APEC model, which takes into account a single-temperature plasma to model the ICM emission. In the fit, parameters for galactic absorption and redshift have been fixed to the original values assumed to produce the observations, while the other parameters were allowed to vary.

For all the clusters in the sample, the best-fitting spectral model generally indicates a very low value of the total metallicity of the plasma. This result is simply reflecting the treatment of the star formation and metal production in the original input simulations, which does not follow proper stellar evolution and injection of metal yields according to proper stellar lifetimes.

We note that, even though the ICM in the clusters is most likely constituted by a multiphase plasma, the single-temperature fit results overall in reasonable estimations, for all the clusters in our sample, as confirmed by the χ^2 statistics (see Fig. A1 in Appendix A). From the distribution of the reduced-χ^2 values, we have in fact $\chi^2 < 1.2$ for ~70 per cent of the clusters in the sample.

4 RESULTS

In this section, we present the X-ray properties and scaling relations of the 179 galaxy clusters in the sample, at $z = 0.11$, obtained from *Chandra* synthetic observations.

---

[1] The MUSIC-2 data base is publicly available at http://music-data.ft.uam.es/, as well as initial conditions.

[2] For the X-ray analysis with the photon simulator, the snapshot $z = 0$ is excluded for technical reasons, since it would imply a formally null angular-diameter distance and, consequently, divergent normalizations of the X-ray model spectra (i.e. infinitely large flux).

[3] See http://heasarc.gsfc.nasa.gov/xanadu/xspec/

[4] for some clusters the band was actually restricted to a smaller energy band, depending on the quality of the spectrum.
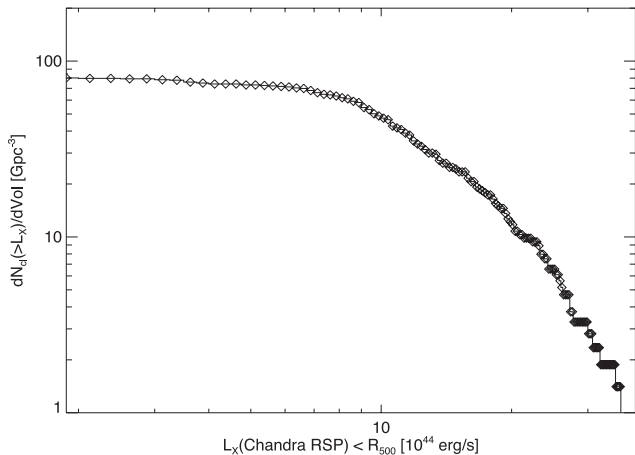
Figure 1. Cumulative luminosity function for the sample of clusters.

4.1 X-Ray properties of the massive haloes

Two interesting, global X-ray properties that we can directly extract from spectral analysis are the luminosity and temperature of the ICM within the projected R_{500}.

4.1.1 The X-ray luminosity

From the theoretical best-fitting model to the synthetic data, we calculate X-ray luminosities for the sample clusters in the entire $0.5-10$ keV band, as well as in the soft and hard X-ray bands, i.e. $0.5-2$ keV and $2-10$ keV, respectively (rest-frame energies).

Furthermore, we extrapolate the total X-ray luminosity to the maximum energy band defined by the *Chandra* response matrix, i.e. $0.26-12$ keV ($0.28-13.3$ keV rest frame). Hereafter, we will refer to this quantity as the 'bolometric' X-ray luminosity.

In Fig. 1, we show the cumulative luminosity function built from the 'bolometric' X-ray luminosity within R_{500} of all the clusters in the sample, $dN(>L_X)/d$ Vol (for a volume corresponding to the simulation box volume).

4.1.2 The X-ray temperature

From the analysis of the *Chandra* synthetic spectra, we also measure the projected mean temperature within R_{500}. All the clusters of the sample have temperatures $T_X > 2$ keV. This temperature, usually referred to as 'spectroscopic' temperature can be compared to the temperature estimated from the simulation as

$$T_w = \frac{\Sigma_i w_i T_i}{\Sigma_i w_i}, \qquad (1)$$

where the sums are performed over the smoothed particle hydro-dynamics (SPH) particles in the considered region of the simulated cluster. The temperature associated with the single gas particle (T_i) is computed taking into account the multiphase gas description following the model by Springel & Hernquist (2003).

The weight w in equation (1) changes according to different theoretical definitions.

As commonly done, we consider:

(i) the mass-weighted temperature, T_{mw}, where $w_i = m_i$;
(ii) the emission-weighted temperature, T_{ew}, where the emission is $\sim\rho^2\Lambda(T) \sim \rho^2\sqrt{T}$ (the cooling function can be approximated by

$\Lambda(T) \sim \sqrt{T}$ for dominating thermal bremsstrahlung), and therefore $w_i = m_i\rho_i\sqrt{T_i}$;

(iii) the spectroscopic-like temperature, T_{sl}, where $w_i = m_i\rho_i T_i^{-3/4}$ (which was proposed by Mazzotta et al. 2004, as a good approximation of the spectroscopic temperature for systems with $T \gtrsim 2$–3 keV).

While computing the emission-weighted and spectroscopic-like temperatures, we apply corrections to the particle density that account for the multiphase gas model adopted (consistently to what is done while generating the X-ray synthetic emission), and we exclude cold gas particles, precisely those with temperatures <0.5 keV.

Among the aforementioned theoretical estimates, the mass-weighted temperature is the value that most-closely relates to the mass of the cluster, directly reflecting the potential well of the system.

Nevertheless, the various other ways of weighting the temperature for the gas emission (such as T_{ew} or T_{sl}) have been introduced in order to better explore the X-ray, observable properties of simulated galaxy clusters and to ultimately compare against real observations. Differences among these definitions and their capabilities to match the observed X-ray temperature have been widely discussed in the literature (e.g. Mathiesen & Evrard 2001; Mazzotta et al. 2004; Rasia et al. 2005; Valdarnini 2006; Nagai et al. 2007).

From the comparison shown in Fig. 2, we also remark the differences existing among the theoretical estimates and the expected spectroscopic temperature T_X, derived from proper spectral fitting. The spectroscopic temperature refers, in this case, to the region within the *projected* R_{500}, which might introduce deviations due to sub-structures lying along the l.o.s. Despite this, we expect it to be fairly consistent to the global, 3D value, given the large region considered.

In Fig. 2, the ratio T_X/T_{sim} is presented as a function of the true cluster mass within R_{500}, M_{500}.

Comparing to the 1:1 relation (black, dot–dashed line in the figure), we note that there are discrepancies among the values. Overall, we conclude from this comparison that T_X tends to be generally higher than the value of T_{sl}. Also, in perfect agreement to the findings of previous works (e.g. Mazzotta et al. 2004), the spectroscopic temperature T_X is on average lower than the emission-weighted estimate.
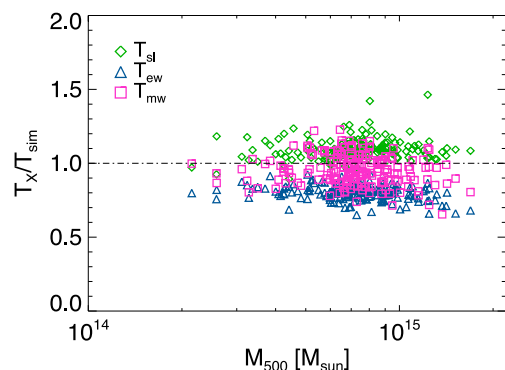

Figure 2. Relations between the X-ray-derived temperature, obtained from spectral fitting of the synthetic spectra in the (0.5–10) keV band, and the different theoretical definitions of temperature estimated directly from the simulation: T_{mw} (mass-weighted, magenta squares), T_{ew} (emission-weighted, blue triangles), T_{sl} (spectroscopic-like, green diamonds). Temperature ratios are plotted as function of the cluster mass within R_{500} (M_{500}).

It is interesting to notice that in our case the discrepancy between T_X and the true, dynamical temperature of the clusters, T_{mw}, is smaller than the deviation from either emission-weighted or spectroscopic-like temperatures.

Nonetheless, with respect to the mass-weighted value, we find that T_X tends to be slightly biased low. On the one hand, this underestimation of the true temperature by the X-ray-derived measurement might be ameliorated via a further exclusion a posteriori of cold, gaseous sub-structures in the ICM. On the other hand, a complexity in the thermal structure of the ICM can persist (for instance, a broad temperature distribution, or a significant difference in the temperatures of the two most prominent gas phases) and eventually affect the resulting X-ray temperature, especially when a single-temperature component is fitted to the integrated spectrum.

As a test, we checked for the dependency of the bias on the χ^2_{red} of the fit and found that there is a mild correlation (see Fig. A2 in Appendix A). Precisely, to higher χ^2_{red} values of the one-temperature spectral fit, correspond on average lower T_X/T_{mw} ratios (and similarly for T_X/T_{ew}). Comparing T_X to T_{sl} this effect basically disappears, confirming that they are almost equally sensitive to the complexity of the ICM thermal distribution.

The observed underestimation of the true temperature by T_X is in agreement with findings from, e.g. early studies using mock X-ray observations of simulated clusters by Mathiesen & Evrard (2001), but there is instead some tension with respect to other numerical studies (e.g. Nagai et al. 2007; Piffaretti & Valdarnini 2008). Nevertheless, as reported also by Kay et al. (2012), who found results consistent with what observed in MUSIC clusters, the discrepancy might be due to the additional exclusion of resolved cold clumps in the X-ray analysis.

In fact, for the set of MUSIC clusters, we observe that a two-temperature model would generally improve the quality of the fit (especially for the objects where the single-temperature fit provides $\chi^2_{red} > 1.2$), better capturing the local multiphase nature of the gas. However, the best-fitting hotter component tends to *over*estimate the mass-weighted temperature, introducing even in this case a significant bias in the results. Moreover, this increases the overall scatter, particularly for colder, low-mass systems, where it is more difficult to distinguish between the two temperature components. Therefore, we decide to consider throughout the following analysis the results from the single-temperature best-fitting models.

Another, more quantitative, way of comparing the deviations of T_{sl}, T_{ew} and T_{mw} from T_X is by confronting the distributions of the bias, defined as

$$b = \frac{T_X - T_{sim}}{T_{sim}}, \tag{2}$$

shown in Fig. 3.

From this, we clearly observe that the distribution of b for $T_{sim} \equiv T_{mw}$ shows the best agreement with the 1:1 relation, although it is not symmetrical and rather biased towards negative deviations. This corresponds to an average underestimation by T_X of ∼5 per cent, over the all sample. More specifically, we find that for almost ∼67 per cent of the clusters considered T_X underestimates the true temperature of the system.

Emission-weighted and spectroscopic-like temperatures suggest instead more extreme differences and narrower distributions. T_{ew} indicates a more significant mismatch with the X-ray value, which tends to be smaller by a factor of ∼20 per cent, with little dispersion. T_{sl} is instead closer to the X-ray temperature, although the distribution of the deviations is slightly biased to positive values of b, indicating a typical overestimation by T_X of a few per cent.
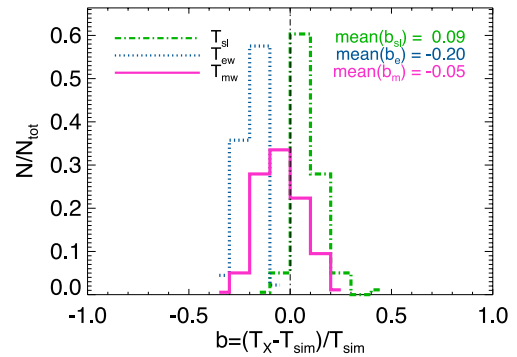

Figure 3. Distribution of the deviations of the X-ray temperature from the simulation estimates, according to the three theoretical definitions: T_{mw} (solid), T_{ew} (dotted), T_{sl} (dash–dotted). Colours as in Fig. 2. The distributions are normalized to the total number of clusters in the sample. Mean value and standard deviation of each distribution are (0.09 ± 0.07) for $T_{sim} \equiv T_{sl}$; (-0.20 ± 0.05) for $T_{sim} \equiv T_{ew}$; (-0.05 ± 0.10) for $T_{sim} \equiv T_{mw}$.

The mean value of each bias distribution is reported in the legend of Fig. 3.

4.1.3 Dependence of the temperature bias on the dynamical state

In order to investigate further the bias in the temperature estimation, we concentrate particularly on the bias between spectroscopic and mass-weighted values, i.e. $b_m = (T_X - T_{mw})/(T_{mw})$ (see equation 2), and explore its relation to the global, intrinsic state of the cluster. To this scope, we calculate from the simulations the centre-of-mass off-set, defined as

$$\Delta r = \frac{\|r_\delta - r_{cm}\|}{R_{vir}}, \tag{3}$$

namely the spatial separation between the maximum density peak (r_δ) and the centre of mass (r_{cm}), normalized to the cluster virial radius (R_{vir}). The choice to adopt this value to discriminate between *regular* and *disturbed* clusters is related to the search for a quantity able to describe the intrinsic state of the cluster, taking advantage of the full three-dimensional information available in simulations. The threshold adopted to divide the clusters into two sub-samples is the fiducial value of $\Delta r_{th} = 0.1$ (see e.g. D'Onghia & Navarro 2007). This represents an upper limit in the range of limit values explored in the literature (D'Onghia & Navarro 2007; Macciò et al. 2007; Neto et al. 2007; Knebe & Power 2008). In our case, given the presence of the baryonic component, we decide in fact to allow for a less stringent criterion (see also Sembolini et al. 2013b).

In Fig. 4, we show the results of this test. The relation between observed bias and Δr is shown in the left-hand panel of the figure. The vertical dashed line marks the separation threshold between regular and disturbed clusters. We note that there is indeed a dependence of the $T_X - T_{mw}$ bias on the dynamical state of the cluster, with a general tendency for b_m to increase with increasing level of disturbance, quantified by the centre-of-mass off-set. More specifically, it is more negative for higher values of Δr. The filled circle and asterisk, and shaded areas, corresponding to the mean values and standard deviations for the two sub-samples, show indeed that the bias distribution is centred very close to zero for the regular clusters, while a more significant off-set is evident for the disturbed sub-sample. The bias distributions for the two sub-samples are shown more clearly in the right-hand panel of Fig. 4 and compared to the global distribution. We note that, the bias calculated
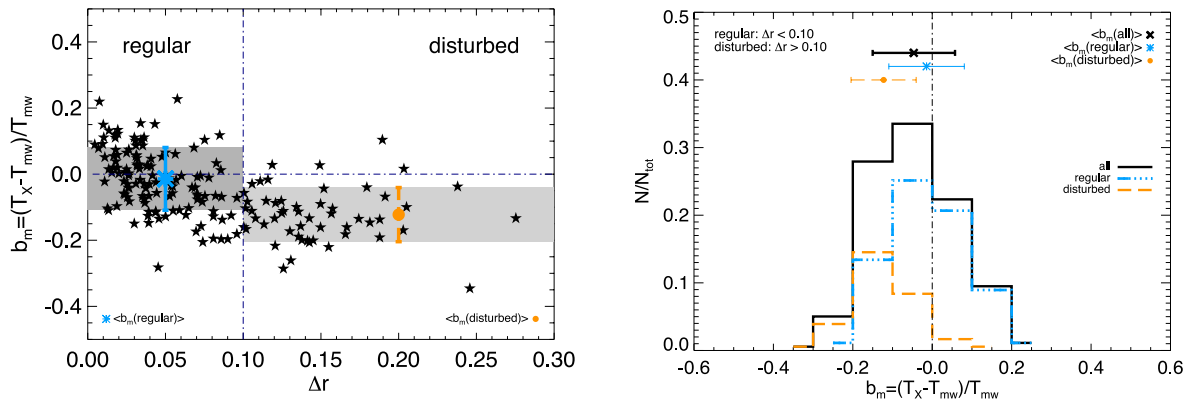
Figure 4. *Left-hand panel:* dependence of the temperature bias ($b_m = (T_X - T_{mw})/(T_{mw})$) on the dynamical state of the cluster, quantified by the centre-of-mass off-set (Δr). The dot–dashed vertical line marks the threshold chosen to separate regular clusters from disturbed ones. In each region of the plot, the mean value of the bias b_m and standard deviation are marked with a symbol (blue asterisk for regular clusters, orange filled circle for disturbed ones) and a shaded area. *Right-hand panel:* the distribution of the bias b_m is reported for the complete sample (black, solid line) and the regular (blue, dot-dot-dot–dashed line) and disturbed (orange, dashed line) sub-sets. Also, the mean values, with 1σ errors, are reported for the three cases (black x, blue asterisk, orange filled circle, respectively).

for the entire sample is basically dominated by the regular clusters, which constitute the majority of the haloes, given the threshold value adopted for Δr. In particular, we find that for regular clusters T_X approximates to a few per cent, on average, the true temperature of the cluster: $\langle b_m(\text{regular})\rangle = -0.01 \pm 0.01$. The disturbed clusters, instead, are characterized by $\langle b_m(\text{disturbed})\rangle = -0.12 \pm 0.01$, indicating a stronger underestimation.

Despite the difference in the mean values, we remark that the distributions of the two populations are quite broad with respect to the bias, as quantified by the standard deviations and shown also in Fig. 4 ($\sigma_{b_m}(\text{regular}) = 0.10$ and $\sigma_{b_m}(\text{disturbed}) = 0.08$).

4.2 Global scaling relations

In this section, we focus on cluster global scaling relations. We consider correlations among X-ray quantities measured from the synthetic PHOX observations (e.g. L_X, T_X), properties estimated from the thermal SZ signal and intrinsic quantities obtained from the numerical, hydrodynamical simulation data directly.

Also, we aim to compare our findings with both current observational results and theoretical expectations from the gravity-dominated scenario of cluster self-similarity.

In this simplified model, the gravitational collapse giving birth to clusters of galaxies determines entirely the global scaling of the system observable properties. Precisely, the gas is assumed to be heated by the gravitational process only, therefore depending uniquely on the scale set by the system total mass (i.e. by the depth of its potential well), and on the redshift (see Kaiser 1986). Under these assumptions, power-law correlations for each set of observables (Y, X) are expected, namely

$$Y = C(X)^\alpha, \tag{4}$$

where C and α are the normalization and the slope of the relation, respectively. Throughout the following, we fit the data with linear relations in the log–log plane[5] of the general form

$$\log(Y) = B + \alpha\log(X), \tag{5}$$

with $B = \log C$.

---

[5] According to our notation, $\log \equiv \log_{10}$.

The slope and the normalization are recovered via a minimization of the residuals to the best-fitting curve (further details on the minimization method adopted will be provided on a case-by-case basis, in the following sections).

Under this formalism, we also calculate the scatter in the Y variable as

$$\sigma_{\log Y} = \left[\frac{\Sigma_{i=1}^N [\log(Y_i) - (B + \alpha\log(X_i))]^2}{N - 2}\right]^{1/2}, \tag{6}$$

where N is the number of data points (for our analysis this is $N = 179$, i.e. the number of clusters in the sample).

4.2.1 Relation between temperature and mass

Here, we discuss the relation between temperature and total mass for the sub-sample of the MUSIC-2 clusters analysed in this work. This is displayed in the left-hand panel of Fig. 5.

The differences that appear while comparing the spectroscopic temperature T_X to T_{mw}, T_{ew} and T_{sl}, basically carry the imprints of the differences existing among the three theoretical estimates of temperature calculated directly from the simulations (see Fig. 5, left-hand panel). Although a shift in temperatures is evident for the different data sets in Fig. 5 (left-hand panel), we note that for none of them the spread in temperature shows any strong dependence on mass.

Regarding T_X, we observe that the observational-like temperatures obtained with PHOX appear to be slightly more dispersed than the theoretical values. This might reflect some contamination due to sub-structures residing along the l.o.s. and within the projected R_{500}, as well as the effect of single-temperature spectral fitting. Even though not major, an increase in scatter and in deviation from self-similarity is also expected as an effect of a more observational-like analysis.

Nevertheless, the overall good correlation between mass and X-ray temperature ensures that the latter behaves as a good tracer of the mass of our clusters, even up to R_{500}. This is particularly interesting as the temperature is derived from the cluster X-ray emission, while the mass considered here is the true mass calculated from the simulation.
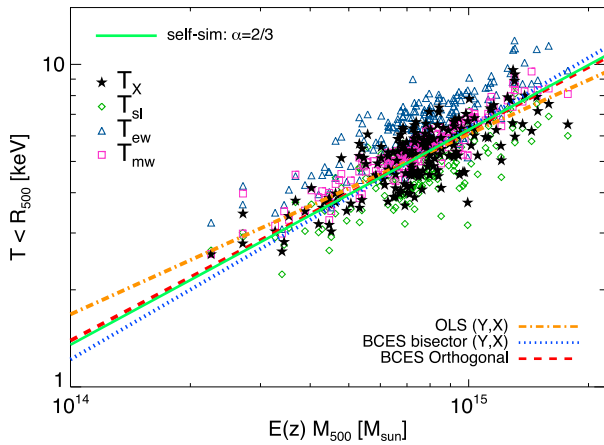
Figure 5. *Left:* temperature–mass relation. Open symbols refer to the three standard definitions of temperature used in simulations: T_{mw} (magenta squares), T_{ew} (blue triangles), T_{sl} (green diamonds). Black stars refer to the X-ray temperature, T_X, extracted from the synthetic spectra in the (0.5-10) keV band. Overplotted in orange the (OLS) best-fitting relation for the T_X-M_{500} relation. For comparison, we also report the bisector and orthogonal best-fitting curves (as in the legend) and the self-similar line, normalized to the data at 7.5×10^{14} M$_\odot$, in mass. *Right:* distribution of the residuals in the T_X-M_{500} relation (in $\log T_X$).

As a step further, we recover the best-fitting relation between the spectroscopic temperature T_X and M_{500}. As in equation (5), we fit the data in the log–log plane using the functional form
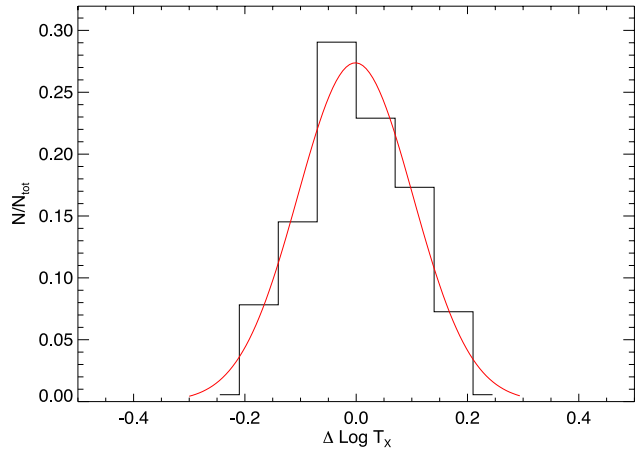
$$\log(T_X) = \log(C) + \alpha \log(E(z) M_{500}), \tag{7}$$

in order to recover slope and normalization of the T_X-M_{500} scaling law.

In equation (7) (and hereafter), the function $E(z)^2 = \Omega_{M,0}(1 + z)^3 + \Omega_\Lambda$ accounts for the redshift and the cosmology assumed.

In this case, we proceed with a simple ordinary least-squares (OLS) minimization method to calculate the slope and normalization of the relation, since the mass is here the intrinsic, true value obtained from the simulation, and therefore, it should be treated as the 'independent' variable. As a result, we find a shallower slope ($\alpha = 0.56 \pm 0.03$) than predicted by the self-similar model ($\alpha_{self-sim} = 2/3$). On the one hand, this shallower dependence might reflect the tendency of T_X to underestimate the true temperature of the system. This is consistent, e.g. with results from numerical studies by Jeltema et al. (2008). On the other hand, the minimization method itself could induce differences in the results, especially when some intrinsic scatter in the relation is present. Indeed, we find a steeper slope when the residuals on both variables are minimized, e.g. via the bisector – $\alpha = 0.72 \pm 0.03$ – or orthogonal – $\alpha = 0.65 \pm 0.04$ – approaches (Bivariate Correlated Errors and intrinsic Scatter – BCES).[6] For the purpose of comparison, we report in Fig. 5 (left-hand panel) the best-fitting curves for all the three methods, as well as the self-similar relation (normalized to the data at 7.5×10^{14} h^{-1} M$_\odot$, in mass).

For this sample, the scatter in $\log T_X$ with respect to the best-fitting relation is some per cent, namely $\sigma_{\log T_X} \sim 0.07$, calculated according to equation (6).

In the right-hand-side panel of Fig. 5, we show the distribution of the OLS residuals for the T_X-M_{500} relation, in $\log T_X$. This can be fitted by a Gaussian function, centred on zero and with standard deviation $\sigma \sim 0.10$.

4.2.2 Relation between luminosity and mass

As well as the temperature, also the X-ray luminosity (L_X) is expected to scale with the cluster mass (see e.g. Giodini et al. 2013, for a recent review on cluster scaling relations). Therefore, we show here the L_X-M_{500} relation for our clusters, within R_{500}. In the case of luminosity, we expect the signature of gas physics to play a major role, introducing both a deviation from self-similarity and a larger scatter. Indeed, the X-ray emission of the ICM is much more sensitive to its thermal state, e.g. to the multitemperature components of the gas and to sub-structures. Furthermore, the implementation of the complex processes governing the gas physics, such as cooling, metal enrichment and feedback mechanisms, can certainly have a non-negligible effect.

Indeed, we observe a steeper correlation than expected and a larger scatter with respect to the temperature–mass relation, $\sigma_{\log L_X} \sim 0.11$ (Section 4.2.1). The best-fitting slope obtained from the OLS minimization method is $\alpha \sim 1.45 \pm 0.05$, with self-similarity predicting $\alpha_{self-sim} = 4/3$. Even though in the same direction, this deviation is however less prominent than for real data (e.g. Maughan 2007; Arnaud et al. 2010).

In Fig. 6, we display the relation and the best-fitting curve. For the purpose of comparison, we also show the self-similar line, normalized in mass to the same pivot used for the best fit, i.e. 7.5×10^{14} h^{-1} M$_\odot$.

4.2.3 Correlations with Y_X

Additionally, it is interesting to address the effects of the measured X-ray temperature with respect to theoretical, intrinsic quantities inferred directly from the simulations. In particular, we report on
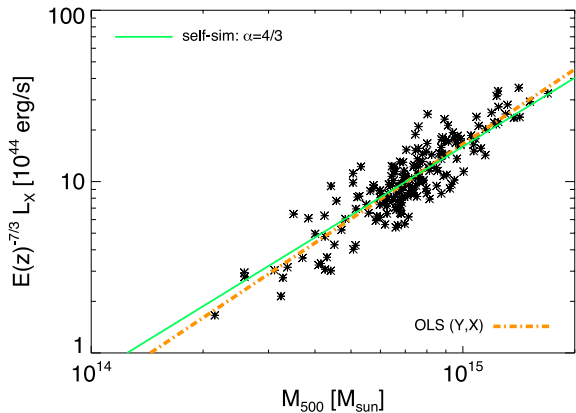
---

[6] We note here that we do not consider errors for the variables directly derived from the simulation (i.e. total mass, gas mass, Y_{SZ}, but also for Y_X), while they are accounted for in the relation between observational quantities, namely T_X and L_X. Nevertheless, we remark that the main important difference with respect to the OLS method is that the bisector or orthogonal approaches, the minimization accounts for the residuals in *both X and Y* variables, therefore providing potentially different best-fitting slopes.

Figure 6. Luminosity–mass relation for the total X-ray band covered by the *Chandra* detector response, to which we refer as 'bolometric' X-ray luminosity. The overplotted dot–dashed, orange curve is the (OLS) best-fitting relation to the data, while the solid green line marks the self-similar relation, normalized to the data at $7.5 \times 10^{14} \, h^{-1} \, M_\odot$, in mass.

the correlations between the total and the gas mass of the clusters, enclosed within R_{500} (M_{500} and $M_{g,500}$, respectively), and the Y_X parameter (introduced by Kravtsov et al. 2006), defined as

$$Y_X = M_g T_X. \tag{8}$$

Y_X basically quantifies the thermal energy of the ICM, and we evaluate it for the cluster region within R_{500}.

The $M_{g,500} - Y_X$ and $M_{500} - Y_X$ relations are shown in the left and middle panels of Fig. 7. Here, we employ the X-ray spectroscopic temperature T_X but still use the true total (M_{500}) and gas ($M_{g,500}$) mass of the simulated clusters, with the sole purpose of calibrating the scaling relations and discerning the effects due to the X-ray (mis)estimate of the ICM temperature.

We confirm that, despite the complexity of the ICM thermal structure, the estimate of temperature derived from X-ray analysis does not influence majorly the shape of the relation with mass and rather preserves the tight dependence. The slope of both relations (0.60 ± 0.01 and 0.58 ± 0.01, respectively) is very close to the self-similar value ($\alpha_{self-sim} = 3/5$) and the scatter in the $\log M$ is only about 4 per cent.

The $L_X - Y_X$ scaling relation (right-hand panel in Fig. 7) shows a steeper ($\alpha \sim 0.94 \pm 0.02$) dependence than expected from self-similarity ($\alpha_{self-sim} = 4/5$). Even in this case, given the expected good correlation between Y_X and the system mass, as well as between temperature and mass, we can ascribe both the larger scatter ($\sigma_{\log L_X} \sim 0.08$, i.e. a factor of ~ 2 larger than in $M_{g,500} - Y_X$ and $M_{500} - Y_X$) and the deviation from the theoretical self-similar model to the L_X observable. Higher values of luminosity for a certain mass can also be affected by the choice of considering the whole region within R_{500}, not excluding the innermost part.

Indeed, we find overall good agreement if compared to similar observational analyses (see e.g. Maughan 2007; Pratt et al. 2009). Nonetheless, this MUSIC-2 sub-sample, sampling the most massive clusters, shows a behaviour slightly closer to self-similarity with respect to the observations.

4.2.4 A pure X-ray scaling relation: $L_X - T_X$

As a further step, we investigate the relation between X-ray luminosity and spectroscopic temperature, within R_{500} (projected radius), for the sample of clusters.

As described in Section 4.1.1, the X-ray luminosity has been obtained from the best fit of the synthetic *Chandra* (ACIS-S) spectra generated with the PHOX simulator, for: 0.5–2 keV (soft X-ray band, SXR), 2–10 keV (hard X-ray band, HXR) and for the total band covered by the ACIS-S detector response ('bolometric' X-ray luminosity). The $L_X - T_X$ for the three aforementioned energy bands is shown in Fig. 8.[7]

In order to study the luminosity–temperature scaling law more quantitatively, we perform a linear fit to the $L_X - T_X$ relation[8] in the log–log plane, in order to find the slope, α, and normalization, C, of the best-fitting relation.

Here, the functional form in equation (5) reads

$$\log(E(z)^{-1} L_X) = \log(C) + \alpha \log(T_X/T_0), \tag{9}$$

where L_X is given in units of 10^{44} erg s^{-1}, as well as the normalization C, and we assume $T_0 = 5$ keV.

For the purpose of comparison, we recall the self-similar expectation for the luminosity–temperature relation:

$$E(z)^{-1} L \propto T^2. \tag{10}$$

The resulting slope and normalization are sensitive to the method adopted to minimize the residuals, so that a cautious interpretation of the two observables involved in the relations is recommended. We notice that, in the particular case of the $L_X - T_X$ relation, we might interpret the luminosity as the 'dependent' variable and the temperature as the 'independent' one, being the latter closely related to the total mass of the cluster (see Fig. 5 and discussion in Section 4.2.1) and therefore tracing an intrinsic property of the system. Under this assumption, the standard OLS method, minimizing only the residuals in the luminosity, would suggest a shallow relation, quite close to the self-similar prediction, with $\alpha = 2.08 \pm 0.07$.

Nevertheless, a more careful approach to find the best-fitting slope consists in a minimization procedure that accounts for both the residuals in L_X and T_X, without any stringent assumption on which variable has to be treated as (in)dependent. Therefore, we apply here the linear regression BCES method, focusing on the bisector (Y, X) and orthogonal modifications (Isobe et al. 1990; Akritas & Bershady 1996). Both methods are in fact robust estimators of the best-fitting slope and provide us with more reliable results than the OLS approach.

For the present analysis, the best-fitting values, with their 1σ errors, and the scatter (see equation 6) are listed in Table 1. We highlight that the scatter of the relation for this MUSIC-2 sub-sample is lower ($\sigma_{\log L_X} \sim 0.11$), with respect to what is usually found when the relation is calculated for a density contrast $\Delta = 500$ (see both numerical and observational studies on the $L_X - T_X$ relation, e.g. Ettori et al. 2004b; Maughan 2007; Pratt et al. 2009; Biffi et al. 2013a,b).

Between the two methods employed, as already pointed out in previous works, the orthogonal BCES provides a steeper best-fitting relation to the data than the bisector (Y, X) method. Nonetheless, the slope of the relation for the MUSIC-2 clusters is found to be in general shallower, and in slightly better agreement to the self-similar prediction, than often observed at cluster scales (e.g. White

---

[7] In the figures, the luminosity is always reported in units of 10^{44} erg s^{-1} and the temperature in keV. We note that errors obtained from spectral fitting are here very small, given the relatively good statistics of photon counts. Hence, for the clarity of the figure, we decide not to show them.

[8] The relation considered for the best-fitting analysis involves the X-ray 'bolometric' luminosity, as in Fig. 8.
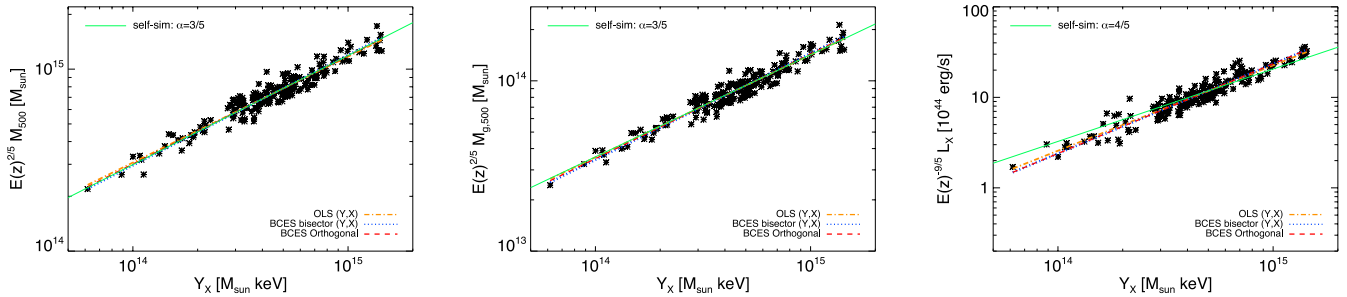
Figure 7. $M_{500}-Y_X$ (left), $M_{g,500}-Y_X$ (middle) and L_X-Y_X (right) scaling relations. Best-fitting lines for the various approaches are reported as in the legend. As a comparison, we also overplot the self-similar predicted curve (solid, green), normalized to the data at $Y_X = 5 \times 10^{14}$ M$_\odot$ keV.
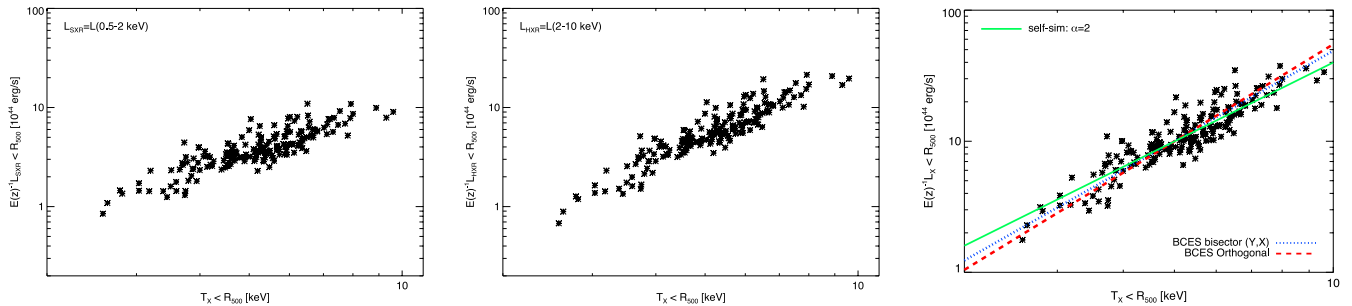

Figure 8. Luminosity–temperature relation for the soft (left-hand panel), hard (middle panel) and 'bolometric' (right-hand panel) X-ray band. *Right-hand panel:* the best-fitting lines for the bisector and orthogonal methods are marked as in the legend, as well as the self-similar curve (green, solid), normalized to the data at the pivot temperature 5 keV.

Table 1. Best-fitting parameters of the L_X-T_X scaling relation: slope, normalization and scatter. The relation is normalized at the value of $T_0 = 5$ keV. For comparison, we also report the expected self-similar slope.

		$\alpha_{\text{self}-\text{sim}}$	α	$C\,(10^{44}\,\text{erg s}^{-1})$	$\sigma_{\log Y_{SZ}}$
[a]L_X-T_X	BCES bisector (Y, X)	2	2.29 ± 0.07	10.03 ± 0.19	0.11
	BCES orthogonal	2	2.46 ± 0.09	9.98 ± 0.19	0.11

[a]The luminosity considered is calculated over the maximum energy band defined by the *Chandra* ACIS-S response, as in Fig. 8.

et al. 1997; Markevitch 1998; Arnaud & Evrard 1999; Ikebe et al. 2002; Ettori et al. 2004b; Maughan 2007; Zhang et al. 2008; Pratt et al. 2009). Here, we notice that the relation is mainly constrained in the high-temperature envelope of the L_X-T_X plane (for all the clusters $T_X > 2$ keV), and we would rather expect a larger statistics in the low-temperature region to introduce a larger deviation from the theoretical expectation. Indeed, a remarkable steepening of the relation is observed especially at galaxy-group scales (or equivalently, for systems with temperatures $< 2-3$ keV), even though this is still a very debated issue (e.g. Ettori et al. 2004a; Eckmiller, Hudson & Reiprich 2011). In agreement with our findings, previous studies indicate a possibly shallower slope that approaches the self-similar expectation for very hot systems (e.g. Eckmiller et al. 2011), which would be the case for the majority of our clusters (see e.g. Fig. 8, where only four objects have 2 keV $< T_X < 3$ keV).

In general, the limitations related to the description of the baryonic physics acting in their central region strongly affect the final appearance of simulated clusters, which still fail to match some observational features. Among these, the L_X-T_X surely represents a critical issue. Certainly, an incomplete description of feedback processes (e.g. from AGN), turbulence (see e.g. Vazza et al. 2009)

and galaxy evolution can weaken the departure of simulated clusters from the theoretical, gravity-dominated scenario and consequently augment the gap between cluster simulations and observations (e.g. Borgani & Kravtsov 2011, for a recent review).

In the case of observed galaxy clusters, in fact, the deviation from the theoretical expectation is often definitely more striking than what is observed for our simulated sample.

As a final remark, we note that the steepening of the MUSIC L_X-T_X relation can also possibly point to the combination of two effects: the effect of temperature underestimation and the possible overestimation of luminosity, artificially increased in the centre because of the incomplete feedback treatment. To this, also the choice of not removing the core from the current analysis can additionally contribute and further investigations in this direction will be worth a separate, dedicated study.

4.2.5 Comparison to SZ-derived properties

We study here correlations between properties of clusters derived from both X-ray synthetic observations and estimates of the SZ signal, in order to build mixed scaling relations for the sample of

MUSIC-2 clusters analysed. Both approaches, in fact, allow us to investigate in a complementary way the properties of the hot diffuse ICM and to assess the effects of the baryonic physical processes on the resulting global features (e.g. McCarthy et al. 2003; da Silva et al. 2004; Bonamente et al. 2006, 2008; Morandi et al. 2007; Arnaud et al. 2010; Melin et al. 2011).

Regarding the SZ effect, of which we only focus here on the thermal component, we recall that the Comptonization y parameter towards a direction in the sky is defined as

$$y = \int n_{\rm e} \frac{k_{\rm B} T_{\rm e}}{m_{\rm e} c^2} \sigma_{\rm T} \, {\rm d}l. \tag{11}$$

A more interesting quantity, however, is the integrated Comptonization $Y_{\rm SZ}$ parameter, which expresses no more a local property but rather describes the global status of the cluster, within a region with a certain density contrast, e.g. $<R_{500}$. As for the estimation of X-ray properties, such global quantity is therefore less dependent on the specific modelling of the ICM distribution.

This is given by

$$Y_{\rm SZ} \equiv \int_\Omega y \, {\rm d}\Omega = D_{\rm A}^{-2} \frac{k_{\rm B} \sigma_{\rm T}}{m_{\rm e} c^2} \int_0^\infty {\rm d}l \int_A n_{\rm e} T_{\rm e} \, {\rm d}A, \tag{12}$$

where $n_{\rm e}$ and $T_{\rm e}$ are electron density and temperature in the ICM, $D_{\rm A}$ is the angular-diameter distance to the cluster and the integration is performed along the l.o.s. (${\rm d}l$ is the distance element along the l.o.s.) and over the solid angle (Ω) subtending the projected area (A) of the cluster on the sky. The other constants appearing in equation (12) are the Boltzmann constant, $k_{\rm B}$, the Thompson cross-section, $\sigma_{\rm T}$, the speed of light, c, and the rest mass of the electron, $m_{\rm e}$.

Simulated maps of the Comptonization parameter y have been generated for the MUSIC clusters, and from them we evaluate the integrated $Y_{\rm SZ}$ within a radius R_{500}, i.e. $Y_{\rm SZ,500}$ (see Sembolini et al. 2013a, for further details). Throughout our analysis, as commonly done, we consider the quantity $Y_{\rm SZ,500} D_{\rm A}^2$ and re-name it as

$$Y_{\rm SZ,500} D_{\rm A}^2 \longrightarrow Y_{\rm SZ}, \tag{13}$$

simply referring to $Y_{\rm SZ}$ hereafter.

As $Y_{\rm SZ}$ has proved to be a good, low-scatter mass proxy [confirmed also by Sembolini et al. (2013a), for the MUSIC-2 data set], it is interesting to explore its relationship with other global cluster properties commonly observed. Precisely, our principal aim is to confront this SZ-derived quantity describing the ICM to global properties obtained instead from the X-ray analysis.

4.2.6 The $Y_{\rm SZ}-T_{\rm X}$ and $Y_{\rm SZ}-L_{\rm X}$ relations

First, we investigate the relation between the integrated Comptonization parameter $Y_{\rm SZ}$ (equation 12, with definition 13) and the X-ray temperature and 'bolometric' luminosity ($T_{\rm X}$ and $L_{\rm X}$) within the projected R_{500} (see e.g. da Silva et al. 2004; Arnaud, Pointecouteau & Pratt 2007; Morandi, Ettori & Moscardini 2007; Melin et al. 2011).

The self-similar scaling of these quantities predicts

$$E(z) Y_{\rm SZ} \propto T^{5/2}, \tag{14}$$

$$E(z) Y_{\rm SZ} \propto (E(z)^{-1} L)^{5/4}. \tag{15}$$

In a more realistic picture, the additional complexity of baryonic processes is most likely responsible for the deviation from the theoretical prediction. Additionally, observational limitations, such as

instrumental response, projection effects and modelling of the data, also play a role in the final shape of reconstructed relations and in the discrepancy with theory.

Also in this case, we fit the synthetic data obtained for the MUSIC-2 clusters assuming a functional form similar to equation (5):

$$\log(E(z) Y_{\rm SZ}) = \log(C) + \alpha \log(X), \tag{16}$$

where $Y_{\rm SZ}$ is the SZ-integrated Comptonization parameter given by equation (12) and re-definition as in equation (13), and the variable X is replaced either with $T_{\rm X}$ (equation 14) or with $E(z)^{-1}L_{\rm X}$ (equation 15). Both the integrated Comptonization parameter $Y_{\rm SZ}$ and the normalization of the relations C are given in units of $\rm Mpc^2$, while the X-ray luminosity and temperature are in units of 10^{44} erg s^{-1} and keV, respectively.

For both these relations, it is not clear which variable between the two quantities involved should be treated as (in)dependent and a simple OLS minimization of the residuals in the Y variable would be most likely inappropriate to provide a reliable fit for the slope. Therefore, in order to correctly approach the problem, we employ also in this case the bisector and orthogonal methods and minimize the residuals of both variables with respect to the best-fitting relation, providing results for both.

We show the scaling relations in Fig. 9 and report the best-fitting values for slope and normalization, together with their 1σ errors, in Table 2. There we also list the scatter (equation 6) around the best-fitting laws ($\sigma_{\log Y} \sim 0.15$ for the $Y_{\rm SZ}-T_{\rm X}$ relation and ~ 0.10 for the $Y_{\rm SZ}-L_{\rm X}$).

From the values listed in Table 2 for the $Y_{\rm SZ}-T_{\rm X}$ relation we notice that the orthogonal BCES method converges on steeper slopes than the bisector method, as in the case of the $L_{\rm X}-T_{\rm X}$ scaling law. In particular, we find that the slope of the $Y_{\rm SZ}-T_{\rm X}$ relation better agrees with the predicted self-similar value than the slope of the $Y_{\rm SZ}-L_{\rm X}$ one, which is equally underestimated by both bisector and orthogonal methods, rather suggesting a slope shallower than the self-similar prediction. Given that $Y_{\rm SZ}$ closely traces the system mass, the deviation of $Y_{\rm SZ}-L_{\rm X}$ from self-similarity can be mainly related to the X-ray luminosity, which is more sensitive to the gas physics and dynamical state than to the temperature, as already shown in previous sections.

Comparing the correlations in Fig. 9, we note that these results are consistent with the departure of the $L_{\rm X}-T_{\rm X}$ scaling law from the self-similar trend previously discussed, which was steeper than theoretically predicted.

Additionally, this behaviour is fairly consistent with other results in the literature, e.g. with findings by da Silva et al. (2004) obtained from numerical simulations as well as with observational studies by Arnaud et al. (2007), Morandi et al. (2007), Melin et al. (2011), Planck Collaboration et al. (2011).

4.2.7 The $Y_{\rm SZ}-Y_{\rm X}$ relation

The cluster integrated thermal energy is quantified both by $Y_{\rm SZ}$ and $Y_{\rm X}$, with the main difference that the former depends on the mass-weighted temperature of the gas, while the latter is rather dependent on the X-ray temperature, resulting more sensitive to the lower entropy gas. These two integrated quantities are therefore expected to correlate tightly, and the comparison allows us to test the thermal state of the ICM and the differences between the true and the X-ray temperature (see e.g. Arnaud et al. 2010; Andersson et al. 2011; Fabjan et al. 2011; Kay et al. 2012).
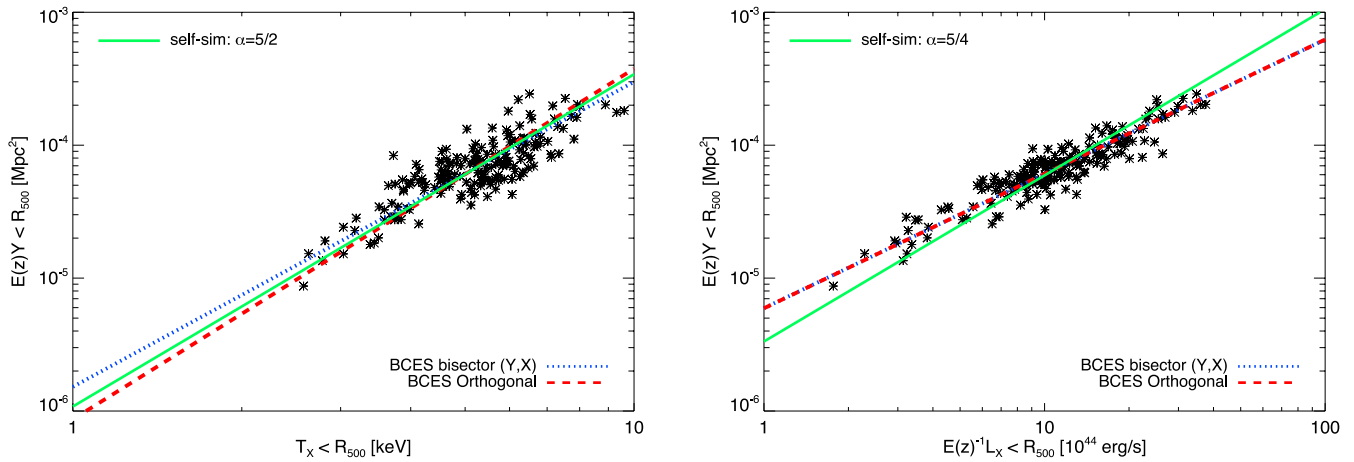
Figure 9. Relations between integrated Comptonization parameter and X-ray temperature and luminosity: $Y_{SZ}-T_X$ (left-hand panel) and $Y_{SZ}-L_X$ (right-hand panel). Best-fitting lines for the bisector and orthogonal approaches are reported as in the legend. Self-similar curves are reported for comparison purposes (green, solid curves), normalized to the data at 5 keV and 10^{45} erg s^{-1} for T_X and L_X, respectively.

Table 2. Best-fitting parameters of the $Y_{SZ}-T_X$ and $Y_{SZ}-L_X$ scaling relations: slope, normalization and scatter. For comparison, we also report the expected self-similar slope.

		$\alpha_{self-sim}$	α	$C\,(10^{-6}\,\mathrm{Mpc}^2)$	$\sigma_{\log Y_{SZ}}$
$Y_{SZ}-T_X{}^a$	BCES bisector (Y, X)	2.5	2.29 ± 0.09	1.52 ± 0.22	0.14
	BCES orthogonal	2.5	2.64 ± 0.12	0.87 ± 0.17	0.16
$Y_{SZ}-L_X{}^a$	BCES bisector (Y, X)	1.25	1.01 ± 0.03	5.95 ± 0.40	0.10
	BCES orthogonal	1.25	1.01 ± 0.03	5.93 ± 0.43	0.10

^{a}The luminosity and temperature considered are those employed in the L_X-T_X relation (see Section 4.2.4).
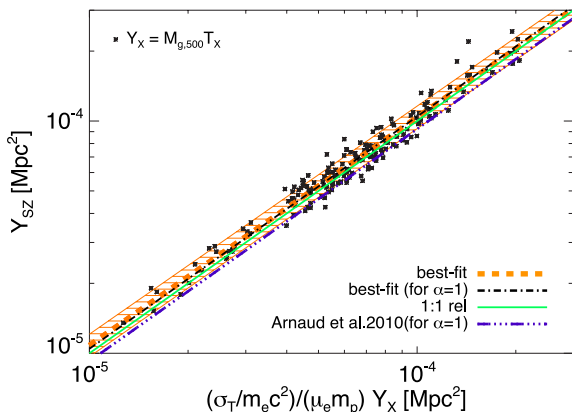

Figure 10. Relation between integrated Comptonization parameter Y_{SZ} and the X-ray-analogue quantity $Y_X = M_{g,500}T_X$. We display in the plot the best-fitting relation to the data (orange, dashed line) and the one obtained by fixing the slope to 1 and fitting for the normalization only (black, dot–dashed), the 1:1 (self-similar) relation (green, solid line) and the observational result by Arnaud et al. (2010; triple dot–dashed, purple line). The shaded orange area marks the 5 per cent scatter about the best-fitting line.

In order to compare directly Y_{SZ} and Y_X, we rescale the latter by the factor

$$C_{SZX} = \frac{\sigma_T}{m_e c^2}\frac{1}{\mu_e m_p} = 1.43 \times 10^{-19}\,\frac{\mathrm{Mpc}^2}{\mathrm{M}_\odot\,\mathrm{keV}} \qquad (17)$$

for a mean molecular weight of electrons $\mu_e = 1.14$.

In Fig. 10, we show the $Y_{SZ}-Y_X$ relation, for the sample of 179 MUSIC clusters with $Y_X = M_{g,500}^{sim}T_X$ (equation 8). By using the

true gas mass within R_{500}, calculated directly from the simulations, we explicitly investigate the role of temperature.

Indeed, since in this case no deviation is included because of the X-ray estimation of the total gas mass, the difference between the 1:1 relation and the best-fitting line is substantially attributed to the misestimation of T_{mw} by T_X. More evidently, the ratio $Y_{SZ}/C_{SZX}Y_X$ can be quantified by the best-fitting normalization of the relation when the slope is fixed to 1.

An ideal measurement of the true temperature of the clusters would basically permit to evaluate by Y_X the very same property of the ICM as done via Y_{SZ}, expecting an actual 1:1 correlation. Dealing with simulated galaxy clusters, this can be tested by employing the true T_{mw} in equation (8). By applying this to our sub-sample of MUSIC clusters, we confirm this with very good precision.

When the spectroscopic temperature is instead employed, for a slope fixed to 1 in the best fit, we observe a higher normalization, $C = 1.05$ (for Y_{SZ} and Y_X both normalized to 5×10^{-4} Mpc^2), with a scatter of roughly 5 per cent. The deviation from 1, $\sim$5 per cent, is consistent with the mean deviation between mass-weighted and X-ray temperatures (see Fig. 3 and discussion in Section 4.1.2). Nevertheless, this deviation is also comparable to the scatter in the relation as, in fact, the T_{mw} and T_X estimates for this MUSIC sub-sample are in very good agreement.

Moreover, we note that the employment of the X-ray temperature generates a larger scatter about the relation, although relatively low with respect to previous (X-ray) relations ($\sigma_{\log Y_{SZ}} \sim 0.05$). This confirms the robustness of Y_X as a mass indicator, despite the minor deviations due to T_X. As a comparison, the ideal, reference test for $Y_X = M_{g,500}T_{mw}$ provides a remarkably tighter correlation, with a scatter smaller than 1 per cent.

Table 3. Best-fitting parameters of the $Y_{SZ}-C_{SZX}Y_X$ scaling relation: slope, normalization and scatter, with different minimization methods. For comparison, we also report the expected self-similar slope.

		$\alpha_{\text{self-sim}}$	α	C^a	$\sigma_{\log Y_{SZ}}$
	OLS (Y, X)	1	0.98 ± 0.01	1.01 ± 0.03	0.05
$Y_{SZ}-C_{SZX}Y_X$	BCES bisector (Y, X)	1	1.00 ± 0.01	1.05 ± 0.03	0.05
	BCES orthogonal	1	1.00 ± 0.01	1.05 ± 0.03	0.05

^{a}Both Y_{SZ} and $C_{SZX}Y_X$ are normalized at the pivot point 5×10^{-4} Mpc^2, so that for the slope fixed to 1, the normalization expresses directly the ratio $Y_{SZ}/C_{SZX}Y_X$.

We also perform the linear fit to the $Y_{SZ}-C_{SZX}Y_X$ in the log–log plane in order to find the values of the slope and normalization that minimize the residuals, listed in Table 3 with the scatter in $\log Y_{SZ}$. Even in this case, both slope and normalization are very close to the expected (self-similar) value of 1, with a scatter of ∼5 per cent.

As marked in Fig. 10 by the orange, dashed curve and shaded area around it (which indicates the 5 per cent scatter), the best-fitting relation for MUSIC clusters is still consistent with the expected one-to-one relation.

4.2.8 Comparison to observational results

Despite the observational-like approach applied to derive X-ray properties, the MUSIC scaling relations still present some differences with respect to observational findings. The aim of this section is to discuss our results, and the level of agreement with previous observational and numerical studies, given the strong sensitivity of X-ray cluster properties to the modelling of the baryonic physics. To this end, we focus on the mass–temperature and luminosity–temperature relations, in order to close the circle between X-ray observables and intrinsic total mass.

(i) $M_{500}-T_X$. In the calibration of the mass–temperature relation, the estimate of T_X plays a role on the normalization as well. In order to investigate this aspect, we show in Fig. 11 the inverse relation $M_{500}-T_X$, as more commonly presented by several authors. The best-fitting curve to the MUSIC data is again fitted, minimizing the residuals in $\log T_X$ (OLS($X|Y$)), as we consider here the true mass of the systems. Consistently with the findings for the T_X-M_{500} scaling relation (Section 4.2.1), the slope here is steeper than self-
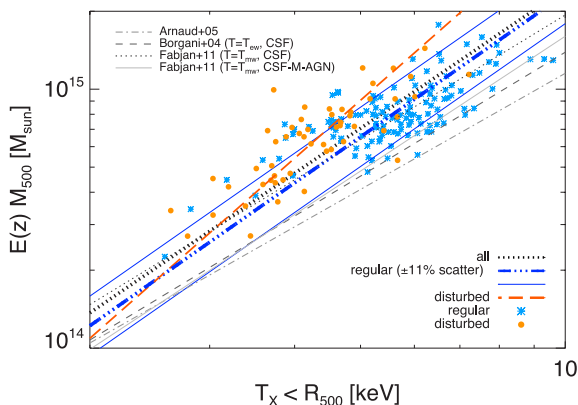

Figure 11. Total mass within R_{500} as a function of temperature. Results are shown considering the X-ray spectroscopic temperature (T_X), for the regular (cyan asterisks) and disturbed (orange circles) sub-samples. Data and best-fitting relations from observations by Arnaud et al. (2005) and from numerical studies by Borgani et al. (2004) and Fabjan et al. (2011) are also shown for comparison.

similar. Moreover, compared to observational data, in particular to the relation by Arnaud, Pointecouteau & Pratt (2005), we find a higher normalization for the MUSIC sample. Part of this difference can be explained by the observational procedure to derive the total mass from the X-rays, which is known to underestimate the true dynamical mass of the system (see early studies by Evrard 1990; Evrard, Metzler & Navarro 1996 and more recent works by Rasia et al. 2006; Nagai et al. 2007; Jeltema et al. 2008; Piffaretti & Valdarnini 2008; Lau, Kravtsov & Nagai 2009; Morandi, Pedersen & Limousin 2010; Rasia et al. 2012; Lau, Nagai & Nelson 2013), i.e. the intrinsic value which is instead used for the MUSIC clusters. Nevertheless, additional effects must play a role in increasing the discrepancy, as this still persists when compared to other numerical works. Namely the treatment of the baryonic physics in the MUSIC simulations can further contribute to this observed off-set, so that, for a fixed mass, the MUSIC clusters appear to be colder. This can be explored, as in Fig. 11, by comparing the MUSIC relation to simulation studies by Borgani et al. (2004) and Fabjan et al. (2011), which also involve the true mass of the systems. In particular, we focus on the sub-sample of MUSIC regular clusters, for which we find on average a very small bias between T_X and T_{mw}. As a consistency check, we compare first against the results by Borgani et al. (2004) and Fabjan et al. (2011) ('CSF'), as they consider the same physical description of the gas as the MUSIC re-simulations, basically including cooling and star formation according to the standard model by Springel & Hernquist (2003). The difference with respect to the former is simply due to the difference in the temperature definition, which is the emission-weighted value in their case; with respect to Fabjan et al. (2011) ('CSF'), where T_{mw} is used instead, we find indeed agreement between the two relations, within the scatter. When the MUSIC data are instead compared to the results by Fabjan et al. (2011) for runs including metal cooling and AGN feedback ('CSF-M-AGN'), we find a larger, although not prominent, deviation. As the mass considered is always the total intrinsic value from the simulation and T_X in MUSIC clusters is close to the T_{mw} estimate, we expect the discrepancy to be mainly due to the different models included to describe the baryonic processes.

(ii) L_X-T_X. Dealing with X-ray properties, the other fundamental quantity taken into account is the luminosity and its relationship with temperature. While the steepening of the MUSIC L_X-T_X relation seems consistent, albeit weaker, with observational results, the normalization is higher than observed. In this case, even though some differences between the approach adopted with PHOX and other observational procedures exist, the limitations due to the treatment of the baryonic physics are likely to play a more significant role.

In fact, the lack of an efficient way to remove the hot-phase gas basically increases the amount of X-ray emitting ICM. This would be mitigated by the inclusion of AGN feedback, although the stronger effects are expected to be particularly important at group
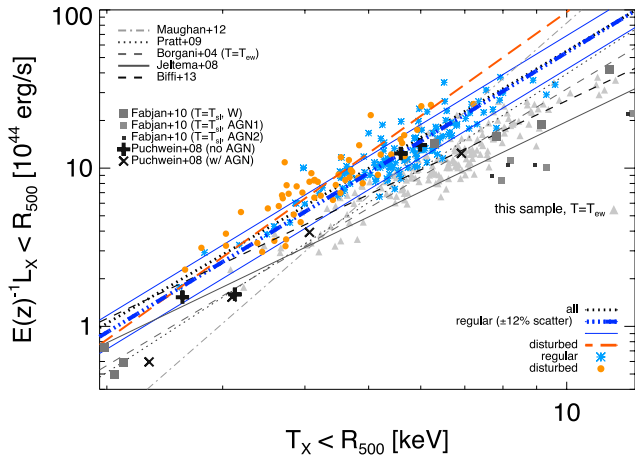
Figure 12. $L_X - T_X$ relation. The results for our sample are presented for both the regular and disturbed sub-sample of clusters (cyan asterisks and orange filled circles, respectively). Values corresponding to the emission-weighted temperature (T_{ew}, light-grey filled triangles) are also shown for comparison, as well as observational data by Maughan et al. (2012) and Pratt et al. (2009) and numerical findings by Borgani et al. (2004), Puchwein et al. (2008), Jeltema et al. (2008), Fabjan et al. (2010) and Biffi et al. (2013b).

scales, while massive clusters like those in our sample ($T_X > 2$ keV) are generally less dramatically affected (as shown by both Puchwein et al. (2008) and Fabjan et al. (2010), despite the different implementations used). In Fig. 12, we show the luminosity–temperature relation for the two sub-samples of regular and disturbed clusters. For comparison, we also report observational data by Pratt et al. (2009), Maughan et al. (2012) and results from numerical studies by Borgani et al. (2004), Jeltema et al. (2008), Puchwein et al. (2008), Fabjan et al. (2010) and Biffi et al. (2013b). In order to minimize the effects due to X-ray temperature bias, we specifically focus on regular MUSIC clusters (for which $\alpha = 2.53 \pm 0.11$ and $C = 9.32 \pm 0.2110^{44}$ erg s^{-1}).

Comparing, we note from Fig. 12 that for a given temperature the MUSIC clusters appear to be generally more luminous. On average, observations (as Pratt et al. 2009; Maughan et al. 2012) predict a luminosity of roughly $6-7 \times 10^{44}$ erg s^{-1}, at $T_0 = 5$ keV, while we find a normalization higher by a factor of $\sim 20-30$ per cent. In fact, the inefficient feedback in the centre can cause higher L_X. With respect to those observational works, the difference can be due in part also to the choice of not removing the core from the current analysis, where the overcooling can affect the cluster central region.

With respect to simulation works employing a spectroscopic temperature, as in the numerical studies by Jeltema et al. (2008), Puchwein et al. (2008) (run with AGN feedback) and Biffi et al. (2013b), or a spectroscopic-like estimate, as in Fabjan et al. (2010) (where the authors use instead T_{sl}), the different normalization of the MUSIC relation must be mainly related to the missing treatment of AGN feedback or proper metal cooling. In fact, our findings are obviously consistent with simulations accounting for similar models of the baryonic processes (as for the run without AGN feedback by Puchwein et al. 2008). This actually explains the diverse level of agreement between the MUSIC clusters and the results by Puchwein et al. (2008) ('w/ AGN' run) and Fabjan et al. (2010) ('AGN1' and 'AGN2' runs), despite they both account for AGN feedback mechanisms.

Instead, the divergence from the best-fitting relation by Borgani et al. (2004) might have a different origin. Notwithstanding the very similar modelling of the gas physics, the authors adopt there a

different definition of the ICM temperature, namely the emission-weighted estimate, which brings the simulated relation closer to both observed results and more complete sets of hydrodynamical simulations (see Jeltema et al. 2008; Fabjan et al. 2010; Biffi et al. 2013b), predicting a luminosity of $\sim 5.6 \times 10^{44}$ erg s^{-1} for $T_0 = 5$ keV. As also confirmed by our analysis, in fact, T_{ew} has been found (e.g. Mazzotta et al. 2004) to overestimate the spectroscopic temperature, which is the one adopted here instead. Similarly, the use of T_{ew} instead of T_X for the MUSIC clusters would also provide a lower normalization ($C = 5.87 \pm 0.1510^{44}$ erg s^{-1}) and a better agreement (see light-grey symbols in Fig. 12).

Additionally, we remark that also numerical resolution can affect the resulting L_X, which can be underestimated in less resolved clusters. Instead, the results tend to reach stability for increasing resolution (see, for instance, Valdarnini 2002). Hence, given the similar physical models treated, the lower normalization of the clusters in Borgani et al. (2004) can also be partially caused by their lower resolution with respect to the MUSIC re-simulations.

The two relations shown in Figs 11 and 12 also provide the case to discuss the behaviour of the regular and disturbed cluster sub-samples. The two groups of objects clearly occupy different regions of the relations, having regular clusters on average higher temperatures. Calculating the two best-fitting curves for the two sub-samples separately, we generally find that disturbed clusters provide steeper relations ($\alpha_{M-T} = \pm$ and $\alpha_{L-T} = 2.96 \pm 0.21$) with respect to regular objects ($\alpha_{M-T} = \pm$ and $\alpha_{L-T} = 2.53 \pm 0.11$). Moreover, the disagreement with previous observational and simulations studies is less significant for the regular sub-set of MUSIC clusters.

The very high statistics of our analysis also provides the case for studying and constraining the scatter of the relations with very good precision, despite the level of agreement in terms of slope and normalization. In fact, the scatter of the L_X-T_X, in particular, is usually significantly larger in real data (up to $50-70$ per cent, as in Pratt et al. 2009; Maughan et al. 2012) than for the MUSIC clusters, where instead $\sigma_{\log L_X} \sim 0.11$. Considering the two subsets separately, the scatter about the best-fitting relation is slightly different, indicating a tighter correlation in the first case and a more dispersed relation in the other, with $\sigma_{\log L_X} \sim 0.10$ (marked by the two solid blue lines in Fig. 12) and $\sigma_{\log L_X} \sim 0.12$, respectively. Similarly, while the scatter of the $M_{500}-T_X$ relation is $\sigma_{\log M} \sim 0.10$ for the whole sample, the dispersion in $\log M$ is found to be smaller for regular objects ($\sigma_{\log M} \sim 0.09$, marked by the two solid blue lines in Fig. 11) and larger for the disturbed ones ($\sigma_{\log M} \sim 0.11$).

5 CONCLUSIONS

This analysis presents results on the largest sample of high-resolution, simulated galaxy clusters ever analysed with observational approach by means of X-ray synthetic observations.

Thanks to the large MUSIC-2 data set, we could obtain a complete volume-limited sample of re-simulated cluster-like objects. Out of these, we select a sub-sample of 179 massive haloes at $z = 0.11$, comprising those matching the mass completeness ($M_{vir} > 7.5 \times 10^{14} h^{-1} M_\odot$) at the considered redshift ($z = 0.11$), but also extending to all the progenitors of the systems with $M_{vir} > 8.5 \times 10^{14} h^{-1} M_\odot$ at $z = 0$. Although restricted to a smaller sub-set, our principal goal with this work is to extend the analysis on the MUSIC-2 clusters (Sembolini et al. 2013a) by addressing their X-ray observable properties and scaling relations.

For all the selected objects, we generated ideal X-ray photon emission (by means of the code PHOX; Biffi et al. 2012) on the base of the gas thermal properties provided by the original

hydrodynamical simulation. From regions up to R_{500} centred on each cluster, we then obtained *Chandra* synthetic observations that provided us with global X-ray properties, such as temperature and luminosity (Section 3).

First, we investigated the bias between the spectroscopic temperature measured from the synthetic spectra (T_X) and the theoretical estimates calculated directly from the simulation.

For the MUSIC sub-sample analysed, T_X is on average lower than the true, mass-weighted value T_{mw}. While this is fairly consistent with studies by Mathiesen & Evrard (2001) and Kay et al. (2008, 2012), we observe some tension with X-ray mock studies of simulated clusters by, e.g. Nagai et al. (2007) and Piffaretti & Valdarnini (2008). This discrepancy can be ascribed to the multiphase thermal structure of the ICM, whose temperature distribution plays an important role in the determination of the global temperature (see also the detailed discussion in Mazzotta et al. 2004). Indeed, a two-component model would improve the description of the multitemperature structure and provide a better spectral fit, albeit with a resulting, evident overestimation of the true temperature by the hotter component of the two. For the generally massive systems considered, this would generate a consequent non-negligible bias. Therefore, we still considered results from the single temperature, keeping in mind the tendency by T_X to a mild, average underestimation of T_{mw}. This difference is very low in our estimates (roughly 5 per cent, despite some dispersion; see Fig. 3) and we confirm an overall good correlation between T_X, within the projected R_{500}, and M_{500} (Fig. 5).

The bias between T_X and T_{mw} is also showing some dependence on the level of dynamical disturbance of the cluster, quantified by the displacement between the system centre of mass and peak of density. Specifically, regular clusters show an average bias which is consistent with zero (basically dominating the result for the entire sample), while the disturbed sub-set presents a more prominent underestimation of T_{mw} by T_X.

The observational-like derivation of the ICM temperature is also useful to investigate possible bias in the correlation with intrinsic properties obtained directly from the simulation, as in the T_X-M_{500} (Section 4.2.1) and $Y_{SZ}-T_X$ (Section 4.2.5) relations. The effect has also been studied via the Y_X, where the observational-like T_X is combined with the true $M_{g,500}$ (Section 4.2.3).

We find that:

(i) T_X-M_{500} shows a larger scatter when T_X is employed rather than T_{mw} and a shallower slope than expected from the self-similar scaling (see Fig. 5);

(ii) $Y_{SZ}-T_X$ is consistent with findings in observational studies, and deviations from self-similarity are less significant than for $Y_{SZ}-L_X$ (Section 4.2.5);

(iii) correlations between Y_X and gas or total mass indicate a slope very close to the self-similar value (Fig. 7);

(iv) the employment of X-ray temperature only affects scatter and normalization of $M_{g,500}-Y_X$ and $M_{500}-Y_X$.

Similar considerations can be drawn when the $Y_{SZ}-Y_X$ scaling law is explored (Section 4.2.7). Here, the normalization is slightly higher than 1, albeit compatible, and the slope is remarkably close to self-similarity (see Table 3). In this case, also the scatter matches the expectation to be very low ($\sigma_{\log Y_{SZ}} \sim 0.05$), although larger than in the ideal case of $Y_X = M_{g,500}T_{mw}$ (where it is $\lesssim 1$ per cent).

Unlike T_X, the X-ray luminosity is intrinsically less accurate to trace mass as it is particularly susceptible to the non-gravitational processes governing the gas physics. In fact, L_X is difficult to model in numerical simulations and, from observations, it is found to add an intrinsic scatter to scaling relations. Here, we confirm that L_X tends to augment the deviation from self-similarity as well as the scatter in the scaling with other intrinsic properties (such as total mass, SZ-integrated Compton parameter or Y_X) and with X-ray temperature.

The L_X-T_X scaling relation for this MUSIC sub-sample extends the study to a larger set of simulated clusters with respect to what previously done with simulations, especially involving a proper generation and derivation of observable X-ray quantities (Puchwein et al. 2008; Fabjan et al. 2010; Biffi et al. 2013a,b). This relation is relatively easy to construct for real clusters as well and generally represents a crucial break of self-similarity. In fact, the observed slope significantly deviates from the self-similar prediction – typically $\alpha \sim 2.5-3$ instead of $\alpha_{self-sim} = 2$ (e.g. White et al. 1997; Markevitch 1998; Arnaud & Evrard 1999; Ikebe et al. 2002; Ettori et al. 2004b; Maughan 2007; Morandi et al. 2007; Zhang et al. 2008; Pratt et al. 2009; Maughan et al. 2012). MUSIC clusters also show a steeper slope than expected, albeit shallower than in real observations (see Table 1), when the residuals are minimized for both variables. Despite the possible deviations in slope and normalization, the increased statistics of this sample allows us to precisely estimate the scatter of the relation, which is found to be only ~ 10 per cent in $\log L_X$.

From the relations explored, we conclude that the interpretation of observational data and comparison to theoretical predictions can certainly benefit from the observational-like approach. In fact, a more faithful comparison is possible even when no additional complications related to the analysis of real data (e.g. background subtraction or spacial changes of the effective area) are included. This is especially true for the slope of the relations, which deviates from self-similarity in a similar way as in observational data.

Differently, the amplitude of the scaling relations is more sensitive to the accuracy of the physical description adopted in hydrodynamical simulations to model the baryonic processes.

In fact, the normalization of MUSIC scaling laws shows more tension with observational findings. We discuss this and the comparison to other simulation works for the $M_{500}-T_X$ and L_X-T_X relations, which represent the two main steps to go from X-ray ICM properties to total mass, via scaling relations. Especially in the L_X-T_X case, we find that the normalization for MUSIC clusters is higher than both observations and more complete simulations. Inefficient cooling and feedback mechanisms, in fact, interplay and compete to moderately increasing the X-ray emitting gas in the central part of MUSIC clusters, thereby augmenting the luminosity and, simultaneously, reducing the temperature.

Certainly, more robust mass indicators that are not strongly affected by non-gravitational processes, such as Y_X, can be safely employed (Kravtsov et al. 2006; Nagai et al. 2007; Fabjan et al. 2011). In fact, the low scatter around the MUSIC $Y_{SZ}-Y_X$, $M_{g,500}-Y_X$ and $M_{500}-Y_X$ relations is preserved, even when we use our observational estimates of the X-ray temperature. Moreover, in the specific case of $Y_{SZ}-Y_X$, the MUSIC clusters are also fairly compatible with observations.

Nevertheless, we remark that, given the increasingly detailed observations available with current and upcoming X-ray instruments (e.g. ASTRO-H and ATHENA+), a more complete modelling of the baryonic physical processes in simulations is required. Unavoidably, this also needs to be combined with a proper observational-like approach to derive X-ray properties. In this way, it will be possible to eventually minimize the distance between numerical hydrosimulations and observations, and correctly interpret the complex, underlying ICM physics.

ACKNOWLEDGEMENTS

REFERENCES

Akritas M. G., Bershady M. A., 1996, ApJ, 470, 706
Allen S. W., Evrard A. E., Mantz A. B., 2011, ARA&A, 49, 409
Andersson K. et al., 2011, ApJ, 738, 48
Arnaud K. A., 1996, in Jacoby G. H., Barnes J., eds, ASP Conf. Ser. Vol. 101, XSPEC: The First Ten Years. Astron. Soc. Pac., San Francisco, p. 17
Arnaud M., Evrard A. E., 1999, MNRAS, 305, 631
Arnaud M., Pointecouteau E., Pratt G. W., 2005, A&A, 441, 893
Arnaud M., Pointecouteau E., Pratt G. W., 2007, A&A, 474, L37
Arnaud M., Pratt G. W., Piffaretti R., Böhringer H., Croston J. H., Pointecouteau E., 2010, A&A, 517, A92
Biffi V., Dolag K., Böhringer H., Lemson G., 2012, MNRAS, 420, 3545
Biffi V., Dolag K., Böhringer H., 2013a, Astron. Nachr., 334, 317
Biffi V., Dolag K., Böhringer H., 2013b, MNRAS, 428, 1395
Bonamente M., Joy M. K., LaRoque S. J., Carlstrom J. E., Reese E. D., Dawson K. S., 2006, ApJ, 647, 25
Bonamente M., Joy M., LaRoque S. J., Carlstrom J. E., Nagai D., Marrone D. P., 2008, ApJ, 675, 106
Borgani S., Kravtsov A., 2011, Adv. Sci. Lett., 4, 204
Borgani S. et al., 2004, MNRAS, 348, 1078
Comis B., De Petris M., Conte A., Lamagna L., De Gregori S., 2011, MNRAS, 418, 1089
D'Onghia E., Navarro J. F., 2007, MNRAS, 380, L58
da Silva A. C., Kay S. T., Liddle A. R., Thomas P. A., 2004, MNRAS, 348, 1401
Eckmiller H. J., Hudson D. S., Reiprich T. H., 2011, A&A, 535, A105
Ettori S. et al., 2004a, MNRAS, 354, 111
Ettori S., Tozzi P., Borgani S., Rosati P., 2004b, A&A, 417, 13
Ettori S., Rasia E., Fabjan D., Borgani S., Dolag K., 2012, MNRAS, 420, 2058
Evrard A. E., 1990, ApJ, 363, 349
Evrard A. E., Metzler C. A., Navarro J. F., 1996, ApJ, 469, 494
Fabjan D., Borgani S., Tornatore L., Saro A., Murante G., Dolag K., 2010, MNRAS, 401, 1670
Fabjan D., Borgani S., Rasia E., Bonafede A., Dolag K., Murante G., Tornatore L., 2011, MNRAS, 416, 801
Gardini A., Rasia E., Mazzotta P., Tormen G., De Grandi S., Moscardini L., 2004, MNRAS, 351, 505
Giodini S., Lovisari L., Pointecouteau E., Ettori S., Reiprich T. H., Hoekstra H., 2013, Space Sci. Rev., 177, 247
Ikebe Y., Reiprich T. H., Böhringer H., Tanaka Y., Kitayama T., 2002, A&A, 383, 773
Isobe T., Feigelson E. D., Akritas M. G., Babu G. J., 1990, ApJ, 364, 104
Jeltema T. E., Hallman E. J., Burns J. O., Motl P. M., 2008, ApJ, 681, 167

Kaiser N., 1986, MNRAS, 222, 323
Kay S. T., Powell L. C., Liddle A. R., Thomas P. A., 2008, MNRAS, 386, 2110
Kay S. T., Peel M. W., Short C. J., Thomas P. A., Young O. E., Battye R. A., Liddle A. R., Pearce F. R., 2012, MNRAS, 422, 1999
Klypin A., Kravtsov A. V., Bullock J. S., Primack J. R., 2001, ApJ, 554, 903
Knebe A., Power C., 2008, ApJ, 678, 621
Komatsu E. et al., 2011, ApJS, 192, 18
Kravtsov A. V., Borgani S., 2012, ARA&A, 50, 353
Kravtsov A. V., Klypin A. A., Khokhlov A. M., 1997, ApJS, 111, 73
Kravtsov A. V., Vikhlinin A., Nagai D., 2006, ApJ, 650, 128
Lau E. T., Kravtsov A. V., Nagai D., 2009, ApJ, 705, 1129
Lau E. T., Nagai D., Nelson K., 2013, ApJ, 777, 151
McCarthy I. G., Babul A., Holder G. P., Balogh M. L., 2003, ApJ, 591, 515
Macciò A. V., Dutton A. A., van den Bosch F. C., Moore B., Potter D., Stadel J., 2007, MNRAS, 378, 55
Markevitch M., 1998, ApJ, 504, 27
Mathiesen B. F., Evrard A. E., 2001, ApJ, 546, 100
Maughan B. J., 2007, ApJ, 668, 772
Maughan B. J., Giles P. A., Randall S. W., Jones C., Forman W. R., 2012, MNRAS, 421, 1583
Mazzotta P., Rasia E., Moscardini L., Tormen G., 2004, MNRAS, 354, 10
Melin J.-B., Bartlett J. G., Delabrouille J., Arnaud M., Piffaretti R., Pratt G. W., 2011, A&A, 525, A139
Meneghetti M., Rasia E., Merten J., Bellagamba F., Ettori S., Mazzotta P., Dolag K., Marri S., 2010, A&A, 514, A93
Morandi A., Ettori S., Moscardini L., 2007, MNRAS, 379, 518
Morandi A., Pedersen K., Limousin M., 2010, ApJ, 713, 491
Morrison R., McCammon D., 1983, ApJ, 270, 119
Nagai D., 2006, ApJ, 650, 538
Nagai D., Vikhlinin A., Kravtsov A. V., 2007, ApJ, 655, 98
Neto A. F. et al., 2007, MNRAS, 381, 1450
Piffaretti R., Valdarnini R., 2008, A&A, 491, 71
Planck Collaboration, 2013, A&A, 550, A129
Planck Collaboration et al., 2011, A&A, 536, A11
Planelles S., Borgani S., Fabjan D., Killedar M., Murante G., Granato G. L., Ragone-Figueroa C., Dolag K., 2014, MNRAS, 438, 195
Prada F., Klypin A. A., Cuesta A. J., Betancort-Rijo J. E., Primack J., 2012, MNRAS, 423, 3018
Pratt G. W., Croston J. H., Arnaud M., Böhringer H., 2009, A&A, 498, 361
Puchwein E., Sijacki D., Springel V., 2008, ApJ, 687, L53
Rasia E., Mazzotta P., Borgani S., Moscardini L., Dolag K., Tormen G., Diaferio A., Murante G., 2005, ApJ, 618, L1
Rasia E. et al., 2006, MNRAS, 369, 2013
Rasia E. et al., 2012, New J. Phys., 14, 055018
Sarazin C. L., 1986, Rev. Mod. Phys., 58, 1
Sembolini F., Yepes G., De Petris M., Gottlöber S., Lamagna L., Comis B., 2013a, MNRAS, 429, 323
Sembolini F., De Petris M., Yepes G., Foschi E., Lamagna L., Gottlöber S., 2013b, preprint (arXiv:e-prints)
Smith R. K., Brickhouse N. S., Liedahl D. A., Raymond J. C., 2001, ApJ, 556, L91
Springel V., 2005, MNRAS, 364, 1105
Springel V., Hernquist L., 2003, MNRAS, 339, 289
Springel V., White M., Hernquist L., 2001, ApJ, 549, 681
Sunyaev R. A., Zeldovich Y. B., 1970, Ap&SS, 7, 3
Sunyaev R. A., Zeldovich Y. B., 1972, Comments Astrophys. Space Phys., 4, 173
Suto D., Kawahara H., Kitayama T., Sasaki S., Suto Y., Cen R., 2013, ApJ, 767, 79
Valdarnini R., 2002, ApJ, 567, 741
Valdarnini R., 2006, New Astron., 12, 71
Vazza F., Brunetti G., Kritsuk A., Wagner R., Gheller C., Norman M., 2009, A&A, 504, 33
White D. A., Jones C., Forman W., 1997, MNRAS, 292, 419
Zhang Y.-Y., Finoguenov A., Böhringer H., Kneib J.-P., Smith G. P., Kneissl R., Okabe N., Dahle H., 2008, A&A, 482, 451

APPENDIX A: EFFECTS ON THE TEMPERATURE ESTIMATE OF THE SINGLE-TEMPERATURE SPECTRAL FIT

We present here the results of the spectral fitting procedure (see Section 3.1), in terms of the reduced-χ^2 statistics, χ^2_{red}.

In Fig. A1, we show the χ^2_{red} distribution (as well as the cumulative one) of the best-fitting single-temperature models for the cluster sample. Additionally, we also show the dependence of the T_X/T_{sim} ratio (see Section 4.1.2) on the fit χ^2_{red}.
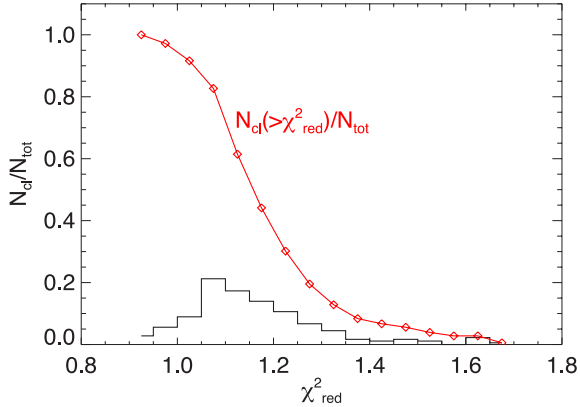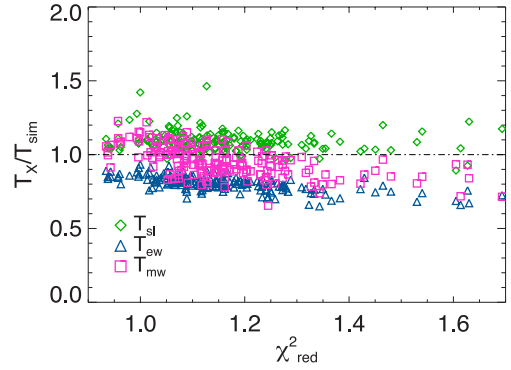

Figure A2. Correlation of the temperature ratio T_X/T_{sim} with the reduced-χ^2 obtained for the single-temperature fit of the cluster *Chandra* spectra. The ratio is reported for the three theoretical estimates of temperature: T_{sl} (green), T_{ew} (blue), T_{mw} (pink). The region considered is always that enclosed by R_{500} and the spectra are fitted over the entire [0.5–10] keV band.

Figure A1. Distribution of the reduced-χ^2 values of the best-fitting models for the clusters in the sample. Overplotted is the cumulative distribution, $N_{cl}(> \chi^2_{red})/N_{tot}$ (solid, red line with diamonds).

This paper has been typeset from a TEX/LATEX file prepared by the author.